fractal and fractional

MDPI

Article

Design of Multi-Cavity Chaotic Maps in the Polar Coordinate Using Nonlinear Curves and Modulo Operation with Application to Cavity-Based Data Hiding

Bo Yan [1,2], Santo Banerjee [3] and Shaobo He [4,*]

[1] School of Informmation Science and Engineering, Shaoyang University, Shaoyang 422000, China; yankebo86@163.com
[2] Provincial Key Laboratory of Informational Service for Rural Area of Southwestern Hunan, College of Information Science and Engineering, Shaoyang University, Shaoyang 422000, China
[3] Department of Mathematical Sciences, Giuseppe Luigi Lagrange, Politecnico di Torino, Corso Duca degli Abruzzi 24, 10129 Turin, Italy; santoban@gmail.com
[4] School of Automation and Electronic Information, Xiangtan University, Xiangtan 411105, China
* Correspondence: heshaobo_123@163.com

Abstract

At present, constructing discrete chaotic systems with unique characteristics and chaos has become a focal topic in the field of nonlinear research. This paper presents a new framework for designing multi-cavity chaotic maps in polar coordinates. It constructs the basic chaotic map through nonlinear curves (such as Lotus curve, rose curves, and star curves) and generates multi-cavity attractors based on modular arithmetic. The nonlinear curves introduce complex deformations in the angular and radial components, while modular arithmetic serves as a folding mechanism to confine the dynamics to a specific range. The combined effect of these two elements forms multiple clearly separated chaotic cavities in the phase space. The number, size, shape, and chaotic characteristics of the cavities can be flexibly controlled by parameters. However, the introduction of fractional-order difference operators will disrupt the multi-chamber structure and make the system more complex. Furthermore, a data-hiding scheme based on the cavities is developed: the cavities act as natural isolation containers to embed information bits, and the chaotic dynamics provide encryption and confusion mechanisms. Experiments show that the designed chaotic map has high complexity and rich bifurcation behaviors; the data-hiding scheme performs well in terms of embedding capacity and security.

Keywords: chaos; complexity; dynamics; fractional difference; data hiding

Check for updates

Academic Editor: António Lopes

Received: 20 April 2026
Revised: 19 May 2026
Accepted: 20 May 2026
Published: 22 May 2026

Copyright: © 2026 by the authors. Licensee MDPI, Basel, Switzerland. This article is an open access article distributed under the terms and conditions of the Creative Commons Attribution (CC BY) license.

1. Introduction

Chaotic systems are renowned for their extreme sensitivity to initial conditions, long-term unpredictability, and ergodicity, holding profound application value in the field of information security, particularly in cryptography and information security applications [1,2]. Their inherent properties make them an ideal choice for generating pseudo-random sequences and concealing the relationship between plaintext information and its covert form [3]. Among various chaotic systems, chaotic maps are widely favored due to their high computational efficiency and ease of implementation [4,5].

During the development of chaotic system design, multi-scroll [6], multi-wing [7], and multi-cavity chaotic systems [8] with higher complexity have attracted much attention due to the complexity of their attractor phase space and topological structure. Among them,

multi-scroll and multi-wing chaotic systems are continuous systems, and the position of the system's equilibrium point is controlled by adjusting the saddle-jump equilibrium point of index 2; while the multi-cavity chaotic system, as a typical discrete system, achieves this by adjusting the position of the iteration point. In the design of multi-scroll and multi-wing chaotic systems, the Chua system [9,10] and Jerk system [11,12] are mainly used as the basis, and nonlinear functions such as sawtooth waves [13] and step waves [14] are employed to regulate the attractor topological structure. As for the multi-cavity chaotic mapping, it is mainly based on the step function to regulate the position of the current or next iteration value, and the step function usually provides a translation function, thereby obtaining a system with a strong discrete attractor. Currently, various types of discrete multi-cavity chaotic maps have been designed, such as the rhombic cavity hyperchaotic map [15], the closed-loop multiple modulation multi-cavity chaotic map [16], and the locally active memristor-based multi-cavity map [17]. Therefore, the construction of new multi-cavity chaotic mapping is still an urgent research topic.

Polar coordinate systems offer a natural framework for describing rotational symmetry and radial variations, which can be leveraged to design chaotic maps with unique topological structures [18,19]. However, many existing chaotic maps defined in polar coordinates often exhibit relatively simple dynamics or limited parameter spaces, potentially restricting their security performance in complex applications like image encryption [20], voice encryption [21], chaotic digital watermarking [22], and data hiding [23]. As a result, designing chaotic maps with controllable, complex structures, such as multiple distinct regions or "cavities", in the Polar coordinate, remains a significant challenge. These multi-cavity structures could provide inherent compartments ideal for embedding secret data. To address these challenges, this paper proposes a novel framework for constructing multi-cavity chaotic maps directly within the polar coordinate system. The core innovation lies in the synergistic integration of nonlinear curves and the modulo operation.

Moreover, nonlinear curves (e.g., Lotus curve, rose curves, and star curves, etc.) can be strategically employed to introduce intricate distortions and deformations to the angular and/or radial components for designing chaotic maps [24]. This manipulation fundamentally alters the trajectory flow, creating complex basins of attraction or repulsion. Secondly, the modulo operation, acting as a folding mechanism, is then crucially applied to confine the dynamics within specific angular or radial intervals. In fact, at present, numerous research efforts are dedicated to designing chaotic maps based on modular operations [25,26], and it has been proven that modular operations can significantly enhance the nonlinearity and complexity of the system. However, in this study, the positive integers obtained through the modulo operation were applied to the system state variables to generate multi-cavity attractors. Information hiding technology refers to embedding specific information into digital host information (such as text, sound, images, video signals, etc.), with the aim of making the hidden information undetectable to the monitor and reducing the possibility of being attacked. It also uses cryptography to enhance security [27–29]. Therefore, information hiding is more secure than information encryption. At present, research on chaotic information hiding technology has made certain progress [30,31]. Although there are currently many multi-scroll, multi-wing, and multi-chamber chaotic system designs, and the complexity of these systems is utilized for data encryption applications [32,33], there is no literature reporting how to use these complex structures for information hiding. It is necessary to conduct further research to fully utilize the characteristics of this complex structure. The main contributions of this work are summarized as follows:

- Six types of polar coordinate chaotic maps are designed based on nonlinear curve functions;

- A novel and generic methodology utilizing the modulo operation for designing multi-cavity chaotic maps in the polar coordinate system is proposed.
- We demonstrate how the parameters of the nonlinear components and modulo operation can be tuned to control the formation, number, and characteristics of the chaotic cavities.
- The preliminary analysis showing that the proposed maps exhibit complex chaotic behavior suitable for cryptographic applications, and evaluate the effectiveness of the cavity-based data-hiding scheme in terms of embedding capacity and security, is carried out.

The remainder of this paper is organized as follows: Section 2: six different kinds of chaotic maps are designed based on the corresponding nonlinear curves; Section 3: details of the proposed methodology for constructing multi-cavity chaotic maps are presented, and systems are simulated; Section 4: complex dynamics of the proposed systems are analyzed; Section 5: a data transmission information hiding scheme based on multi-cavity modulation technology was proposed, and corresponding simulation verification was carried out; Finally, Section 6 concludes the paper and discusses future work.

2. Search for Chaos in Nonlinear Curves

2.1. Nonlinear Curves with Elegant Shapes

The Lotus curve is given by

$$r = R + \frac{1 + 2|\cos(3\theta)| - 4|\sin(3\theta)|}{4 + 16|\sin(6\theta)|}, \tag{1}$$

where R controls the size of the radius, and we also call it the curve one. When $R = 5, 10, 15$, the curves are shown in Figure 1a.

The second curve is defined by

$$r = arc\cos(-0.7\tan(3\theta)\cot(3.6\theta)), \tag{2}$$

and there are no parameters, and we call this curve Curve 2. The curve is shown in Figure 1b.

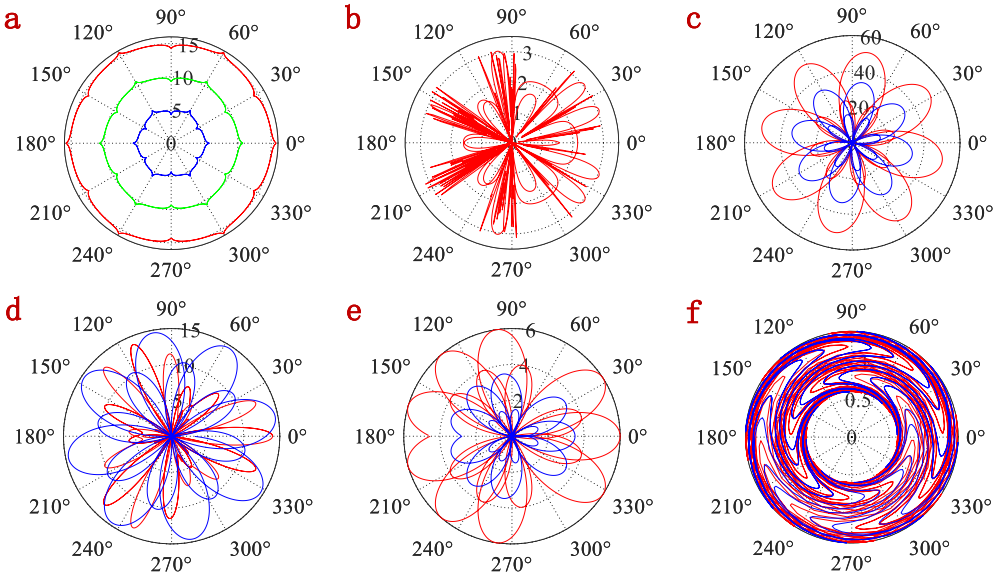


Figure 1. In the polar coordinate system, the graphs of six different curves are presented, where (**a**–**f**) correspond to the curve equations defined by Equations (1)–(6).

The subsequent four curves, designated as curves three through six, are represented by the following equations:

$$r = b_3(2.5\sin(2.66\theta) - \cos(6a_3)), \tag{3}$$

$$r = 9\sin(1.5\theta)\cos(a_4\theta) - b_4, \tag{4}$$

$$r = 1 + b_5\cos(\kappa\theta), \tag{5}$$

and

$$(r, \theta) = (1 + d_6\sin a_6 t, t + c_6\sin b_6 t). \tag{6}$$

It is noted that curve six pertains to a two-dimensional system, where the angle and amplitude are clearly distinguished. When a_3 equals 1.5 and b_3 equals either 15 or 10, the plots of curve three are shown in Figure 1c. When a_4 equals either 8 or 4, b_4 equals 5, the plots of curve four are shown in Figure 1d. When κ equals 11/4 and b_5 equals either 5 or 2.5, the plots of curve five are shown in Figure 1e. When a_6 equals -8, b_6 equals 24, c_6 equals 1.989, and d_6 equals 0.4, the plots of curve six are shown in Figure 1f. Firstly, these equations reveal that the system exhibits significant nonlinear characteristics, primarily induced by various trigonometric functions. Secondly, in polar coordinates, different functions can generate elegant curves with diverse morphologies. Next, we will explore the specific effects of constructing chaotic mappings based on these functions.

2.2. Design of Chaotic Maps

Based on the aforementioned functions, the following are the designs of six different discrete chaotic systems, and they are listed below.

Chaotic map 1 (CM1):

$$y_{n+1} = R \cdot \left[a_1 + \frac{1 + 2|\cos(6y_n)| - 4|\sin(3y_n)|}{4 + 16|\sin(6y_n)|}\right], \tag{7}$$

where R is the control parameter that affects the oscillation range and the input magnitude of the trigonometric function.

Chaotic map 2 (CM2):

$$y_{n+1} = R[\arccos(\sin(-0.7\tan(3y_n)\cot(3.6y_n)))], \tag{8}$$

where the parameter R controls the oscillation amplitude and the input domain of the trigonometric functions.

Chaotic map 3 (CM3):

$$y_{n+1} = R[2.5\sin(2.66y_n) - \cos(6a_3)], \tag{9}$$

where R plays the same role as above, and there is a parameter a_3 in this system.

Chaotic map 4 (CM4):

$$y_{n+1} = 9\sin(1.5y_n)\cos(a_4y_n) - b_4, \tag{10}$$

where a_4 and b_4 are the two system parameters, and since the amplitude is controlled by the coefficient 9.

Chaotic map 5 (CM5):

$$y_{n+1} = R(1 + b_5\cos(\kappa y_n)), \tag{11}$$

where R plays the same role as above, and there are two parameters $\kappa = 11/4$ and b_5 in this system.

Chaotic map 6 (CM6):

$$(r_{n+1}, \theta_{n+1}) = (1 + d_6 \sin a_6\theta_n, r_n + c_6 \sin b_6\theta_n). \tag{12}$$

As a result, CM6 is a two-dimensional system containing four parameters: a_6, b_6, c_6, d_6. Among them, the first dimension primarily controls the angular oscillation of the system in polar coordinates, while the second dimension governs the complexity oscillation of the system in polar coordinates.

In all the above systems, R serves as the control parameter to adjust the oscillation range and the input magnitude of the trigonometric functions, thereby generating chaotic behavior under different parameter values. The system parameters are detailed in Table 1, with all systems exhibiting chaotic characteristics, as demonstrated by their positive Lyapunov exponents. Furthermore, the phase diagrams of each system are presented in Figure 2. In Figure 2a the green, red and blue phase diagrams are plotted using $R = 5, 10, 15$, respectively. Overall, the designed chaotic mapping phase diagrams not only successfully preserve the typical features of the curves but also generate intricate patterns under polar coordinate transformation. This result robustly demonstrates the feasibility and effectiveness of the design schemes.

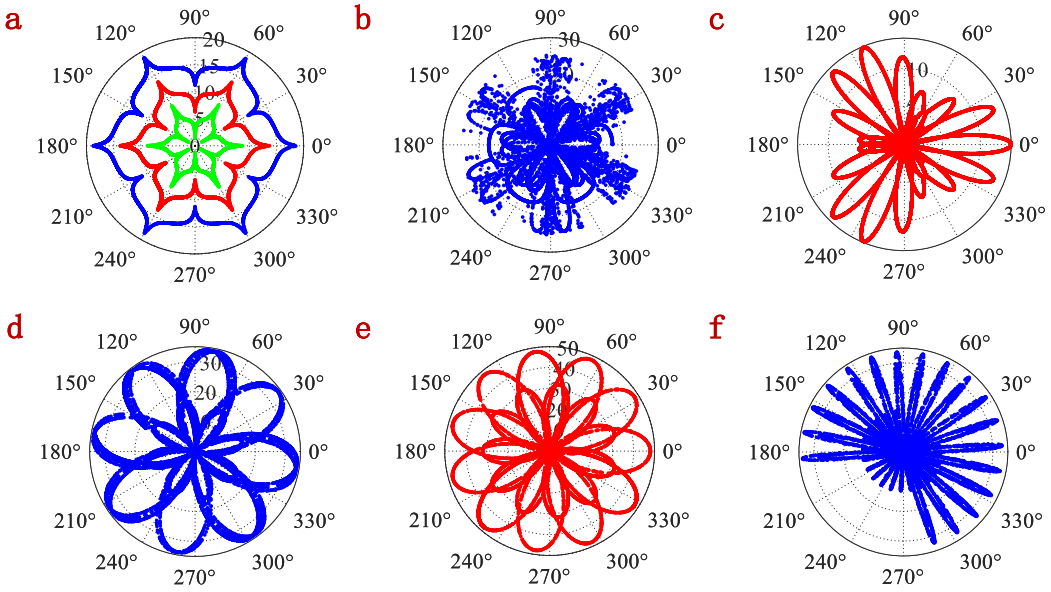


Figure 2. In polar coordinate system, six different phase diagrams of chaotic maps. (**a**) CM1, (**b**) CM2, (**c**) CM3, (**d**) CM4, (**e**) CM5, (**f**) CM6.

Table 1. Parameters, and LEs of six chaotic maps.

Systems	Parameters	LEs
CM1, Equation (7)	$R = 5$, $a_1 = 3$	2.1353
CM2, Equation (8)	$R = 8$	4.0154
CM3, Equation (9)	$R = 10$, $a_3 = 1.5$	3.0317
CM4, Equation (10)	$a_4 = 8$, $b_4 = 5$	3.5034
CM5, Equation (11)	$R = 8$, $b_5 = 5$	3.6847
CM6, Equation (12)	$a_6 = -8$, $b_6 = 24$, $c_6 = 1.989$, $d_6 = 0.4$	3.1762, −2.7413

3. Design Multi-Cavity Chaotic Maps in the Polar Coordinate

The core of this study lies in performing translation operations on points in the initial phase space to form a new distribution of phase space with a multi-cavity structure. Unlike the existing literature's design methods for chaotic maps based on sign functions in Cartesian coordinates, this study proposes a multi-cavity chaotic map design strategy in polar coordinates based on modulo operations. The design methodology of the multi-cavity chaotic map is systematically elaborated, and the corresponding phase diagrams of multi-cavity attractors are presented.

3.1. Design Multi-Cavity Chaotic Maps with Modulo Operation

3.1.1. The Proposed Method

The relationship between the rectangular coordinate system and the polar coordinate system is denoted as

$$\begin{cases} x = r\cos(\theta) \\ y = r\sin(\theta) \end{cases} \Leftrightarrow \begin{cases} r = \sqrt{x^2 + y^2} \\ \theta = \arctan\left(\frac{y}{r}\right) \end{cases}, \tag{13}$$

and the the relationship between the Cartesian coordinate system and the polar coordinate system is also shown in Figure 3. However, special attention must be paid, the value of θ in the above equation is only valid for the scenario illustrated in the figure (located in the first quadrant) (where $\theta \in \left[0, \frac{\pi}{2}\right]$, and the point cannot be the origin). For other quadrants, it needs to be handled according to specific circumstances.

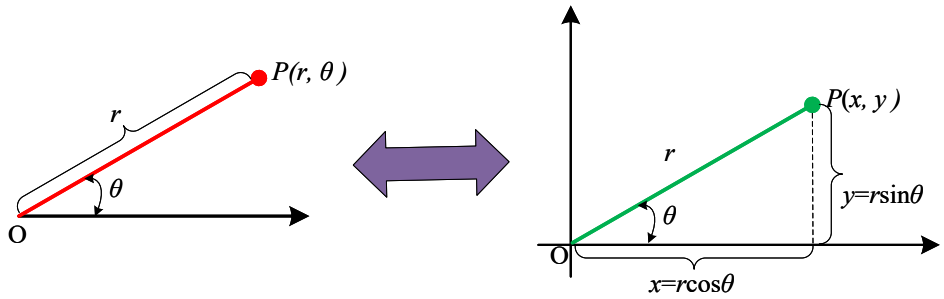


Figure 3. A diagram of the relationship between the Cartesian coordinate system and the polar coordinate system.

When designing polar multi-cavity chaotic mapping, controlling the angle and magnitude is crucial. Compared to the angle, manipulating the magnitude appears more intuitive and straightforward. For one-dimensional chaotic mapping, we can achieve control by embedding a displacement within the system. Although this operation affects both magnitude and angle, the angle—constrained by periodic laws—often exhibits minimal noticeable variation. In contrast, the magnitude value undergoes significant changes with the increase or decrease of the displacement.

To design and obtain multi-cavity chaotic attractors in polar coordinates, it is necessary to establish a displacement mechanism in the r-coordinate direction to control the outward movement of the attractors and achieve hierarchical explicit representation. In this paper,

$$x_{n+1} = f(x_n) + \kappa \cdot h(x_n, m) \tag{14}$$

where $f(\cdot)$ is the nonlinear function of the chaotic map and $h(\cdot)$ is the control function.

$$h(x_n, m) = \mathrm{mod}\left(\lfloor 10^{\sigma} x_n \rfloor, m\right) \tag{15}$$

where σ and m are positive integer numbers, and $\lfloor \cdot \rfloor$ is the round down function. It can be seen that the value of $h(x_n)$ is a positive integer ranging from 0 to $m-1$, and m circles of attractors can be generated.

Remark 1. *For the system to operate properly, the functions that incorporate the variable must be periodic and bounded periodic functions, namely $f(x+kT) = f(x)$, where T is the periodic of the function. In practical applications, many trigonometric functions satisfy this condition.*

Remark 2. *The multi-loop chaotic attractor in polar coordinates is equivalent to the multi-cavity chaotic attractor in the rectangular coordinate system. According to Equation (13), when r changes, x and y will change collaboratively.*

In a polar coordinate system, if it is necessary to construct multi-cavity mapping simultaneously in the radial (r) and angular (θ) directions, precise control of both amplitude and phase must be achieved. This study proposes a multi-cavity mapping construction strategy based on two-dimensional sequences, with the specific process illustrated in Figure 4. Firstly, based on the acquired amplitude and phase sequences (r_n, θ_n), the following transformation is performed, which is

$$\begin{cases} \tilde{r}_n = r_n + \kappa \cdot h(r_n, m_1) \\ \tilde{\theta}_n = \rho \dot{\theta}_n^{Nor} + \frac{2\pi}{m} h\left(\theta_n^{Nor}, m_2\right) \end{cases}, \tag{16}$$

where κ represents the step size in the amplitude direction, the value of which is determined by the span of the attractor. m_1 and m_2 denote the number of cavities in the amplitude and angular dimensions, respectively. θ_n^{Nor} is the value obtained by normalizing θ_n to the interval $[0, 2\pi/m]$, and it is defined by

$$\theta_n^{Nor} = \frac{2\pi}{m} \cdot \frac{\theta_n - \min(\theta_n)}{\max(\theta_n) - \min(\theta_n)}. \tag{17}$$

It shows that the step size in the angular dimension is $2\pi/m$, and the quantity is further regulated by introducing random numbers. In CM6, the variables in polar coordinate form (r_n, θ_n) are directly exported, whereas in a one-dimensional system, the variables (r_n, θ_n) are equivalent to the sequence (y_{n-1}, y_n).

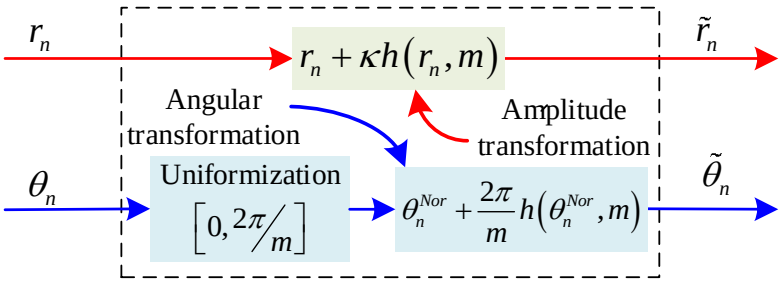


Figure 4. The flow chart of the algorithm for generating grid multi-cavity attractors.

3.1.2. Theoretical Analysis About the Method

Modular arithmetic is a fundamental tool in digital communication and cryptography, transforming values from a continuous or large integer domain into a finite set of integers. Let m be a positive integer (the modulus). Two integers a and b are congruent modulo m, written as

$$a \equiv \bmod(b, m), \tag{18}$$

if m divides $(a-b)$. For any integers a, b and modulus m, the following properties hold:

- Closure: The set $Z_m = \{0, 1, \ldots, m-1\}$ is closed under addition and multiplication modulo m.
- Nonlinearity: The modulo operation is highly nonlinear and sensitive to small input perturbations; $x + \delta$ may produce a completely different residue if δ crosses a multiple of m. This property is crucial for the sensitivity of chaotic key streams.

Overall, the modular and clipping operations are integral to the multi-cavity behaviors.

Take system (11) as an example, in polar coordinates, the state of the system is described by an angular variable $\theta_n \pmod{2\pi}$, which transforms the original one-dimensional map into a circle map. Through the substitution $\theta_n = \kappa y_n \pmod{2\pi}$, the original equation becomes

$$\theta_{n+1} = \kappa R(1 + b_5 \cos(\theta_n)) \equiv A + B\cos(\theta_n) \pmod{2\pi}, \tag{19}$$

where $A = \kappa R$ and $B = \kappa R b_5$. This map is the classic cosine circle map, describing the discrete evolution of the angle θ on the unit circle In the aforementioned discussion on modular arithmetic as given in Equation (18), the assumed moduli were all integers, which are the basic characteristics of modular arithmetic. However, the circle map in Equation (19) employs a real modulus 2π to represent angular periodicity. This is a common way to extend the concept of congruence to the real number range, and the two are not in conflict.

- Nonlinear driving: The cosine term $\cos(\theta_n)$ introduces nonlinearity, making the update of the angle depend on the cosine of the current phase. When $B = 0$, the system reduces to a uniform rotation $\theta_{n+1} = A$, which corresponds to quasiperiodic motion when the rotation number is irrational.
- Frequency locking and resonance: For non-zero B, the system may enter frequency locking (Arnold tongues), i.e., the rotation number $\Omega = \lim_{n\to\infty}(\theta_n - \theta_0)/(2\pi n)$ becomes rational. Fixed points satisfy $\theta = A + B\cos\theta$, corresponding to phase synchronization; their stability is determined by the derivative $|\mathrm{d}\theta_{n+1}/\mathrm{d}\theta_n| = |B\sin\theta|$.
- Route to chaos: As B increases, the system can enter chaos via period-doubling bifurcations, at which point the angular evolution becomes unpredictable, representing the typical chaotic behavior of circle maps.

As a result, in polar coordinates, the system state is intuitively represented as a point on the circle, and the angular evolution directly reflects the periodic, locked, and chaotic behaviors. The parameter κ acts as a spatial scaling factor, while R and b_5 control the base rotation frequency and the nonlinear strength, respectively. This formulation simplifies the global analysis of the system and is a common tool for studying nonlinear oscillations, phase-locked loops, and biological rhythms.

Finally, the quantitative relationship between the cavity number control parameter m and the modulo operation step size κ: $m = \left\lfloor \frac{\Delta r}{\kappa} \right\rfloor + 1$, where Δr is the variation range of the radial component r of the nonlinear curve, which is determined by the nonlinear curve parameters. For example, in the lotus curve, Δr is positively correlated with R, i.e., the larger R is, the larger Δr is.

3.2. Multi-Cavity Chaotic Maps and Simulations

For the five one-dimensional chaotic maps proposed in this study, a random control factor $h(x_n)$ is introduced at the system end to achieve precise control over the displacement of the attractor in the polar coordinate r direction. The corresponding system equations are expressed as follows.

(1) The grid chaotic map 1 (GCM1):

$$y_{n+1} = R\left(a_1 + \frac{1 + 2|\cos(6y_n)| - 4|\sin(3y_n)|}{4 + 16|\sin(6y_n)|}\right) + \kappa_1 h(y_n, m_1). \tag{20}$$

(2) The grid chaotic map 2 (GCM2):

$$y_{n+1} = R[\arccos(\sin(-0.7\tan(3y_n)\cot(3.6y_n)))] + \kappa_2 h(y_n, m_2). \tag{21}$$

(3) The grid chaotic map 3 (GCM3):

$$y_{n+1} = 9\sin(1.5y_{n+1})\cos(a_3 y_{n+1}) - b_3 + \kappa_3 h(y_n, m_3). \tag{22}$$

(4) The grid chaotic map 4 (GCM4):

$$y_{n+1} = R[2.5\sin(2.66y_n) - \cos(6a_4)] + \kappa_4 h(y_n, m_4). \tag{23}$$

(5) The grid chaotic map 5 (GCM5):

$$y_{n+1} = R(1 + b_5\cos(\kappa y_n)) + \kappa_5 h(y_n, m_5). \tag{24}$$

In the aforementioned system, the system parameters remain consistent with those of the original system, and thus will not be reiterated here. For each system, a controller and its corresponding control parameters κ_{1-5} have been subsequently added.

Upon setting the parameter $a_1 = 3$, $R = 5$, $\kappa_1 = 2m_1$, the phase diagram of the GCM1 system, as depicted in Figure 5a, reveals that the system's attractor phase diagrams assume a ring-like configuration contingent upon the m_1 parameter. Specifically, when m_1 is assigned the values of 2, 3, or 4, the system's behavior is characterized by ring-shaped attractor phase diagrams. For the GCM2 system, with parameters $R = 5$, $\kappa_2 = 30$, and m_2 assigned values of 2, 3, or 4, the phase diagram presented in Figure 5b demonstrates that, aside from the attractor positioned at the origin of the coordinate axes, the remaining $m_2 - 1$ attractors are arranged in a ring-like pattern. This outcome suggests that the system is capable of producing ring-shaped attractor phase diagrams that correspond to the m_2 parameter. In the case of the GCM3 system, with parameters $a_3 = 8$, $b_3 = 5$, $R = 5$, $\kappa_4 = 20$, and m_3 taking on values of 2, 3, or 4, the phase diagram illustrated in Figure 5c shows that as m_3 increases, the attractor phase diagrams evolve to display increasingly intricate multi-layered structures, with the number of layers incrementally augmenting. For the GCM4 system, under the parameters $a_4 = 1.5$, $R = 10$, $\kappa_4 = 40$, and with m_4 values of 2, 3, or 4, the phase diagram in Figure 5d indicates that the layers of the attractor phase diagrams proliferate and the structure becomes more complex as m_4 increases. Lastly, for the GCM5 system, with parameters $b_5 = 3$, $R = 8$, $\kappa_5 = 68$, and m_5 values of 2, 3, or 4, the phase diagram in Figure 5e similarly demonstrates that m_5 governs the number of layers in the attractors. As the value of m_5 increases, the attractors exhibit more layers and a more complex structure.

Regarding the CM6 model, as delineated in Equation (12), the parameters are specified as $a_6 = -8$, $b_6 = 24$, $c_6 = 1.989$, and $d_6 = 0.4$. Utilizing the generated sequence (r_n, θ_n), a plurality of cavity attractors are established, with the outcomes of this formation depicted in Figure 6, wherein $m_1 = m_2 = 4, 5, 6, 7$. The figure illustrates that the attractor possesses a multi-chamber configuration within the polar coordinate system. Within this system, the distributions of amplitude and angular directions manifest a reticulated structure, with their hierarchical configurations delineated by parameters m_1 and m_2, respectively. Through

appropriate transformations, it is possible to construct chaotic attractors characterized by multi-directional discretization within the polar coordinate system.

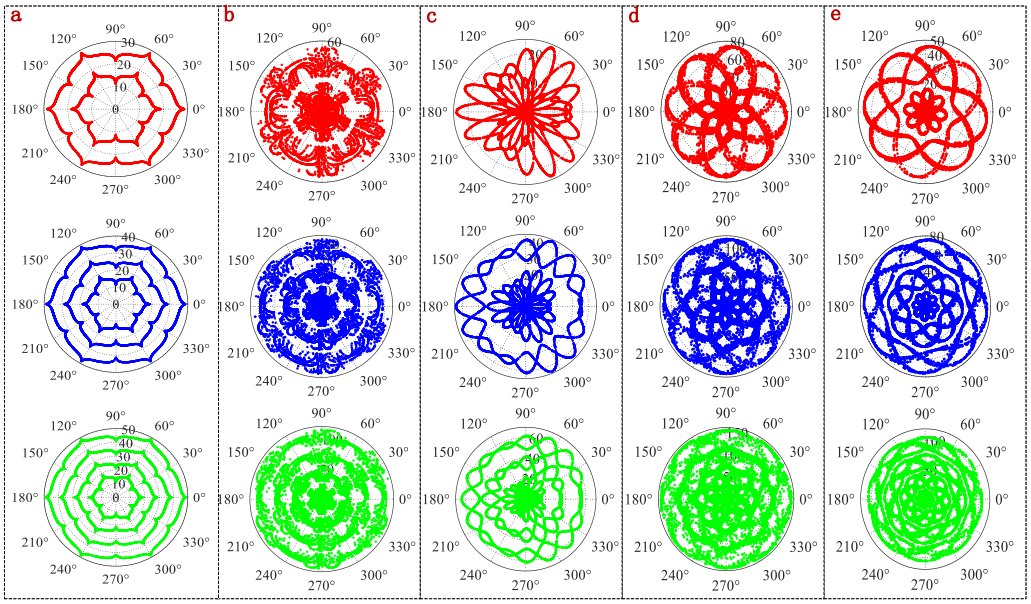


Figure 5. The varying quantities of multi-cavity chaotic attractors within distinct systems are distributed along the radial axis of polar coordinates. (**a**) GCM1, (**b**) GCM2, (**c**) GCM3, (**d**) GCM4, (**e**) GCM5.

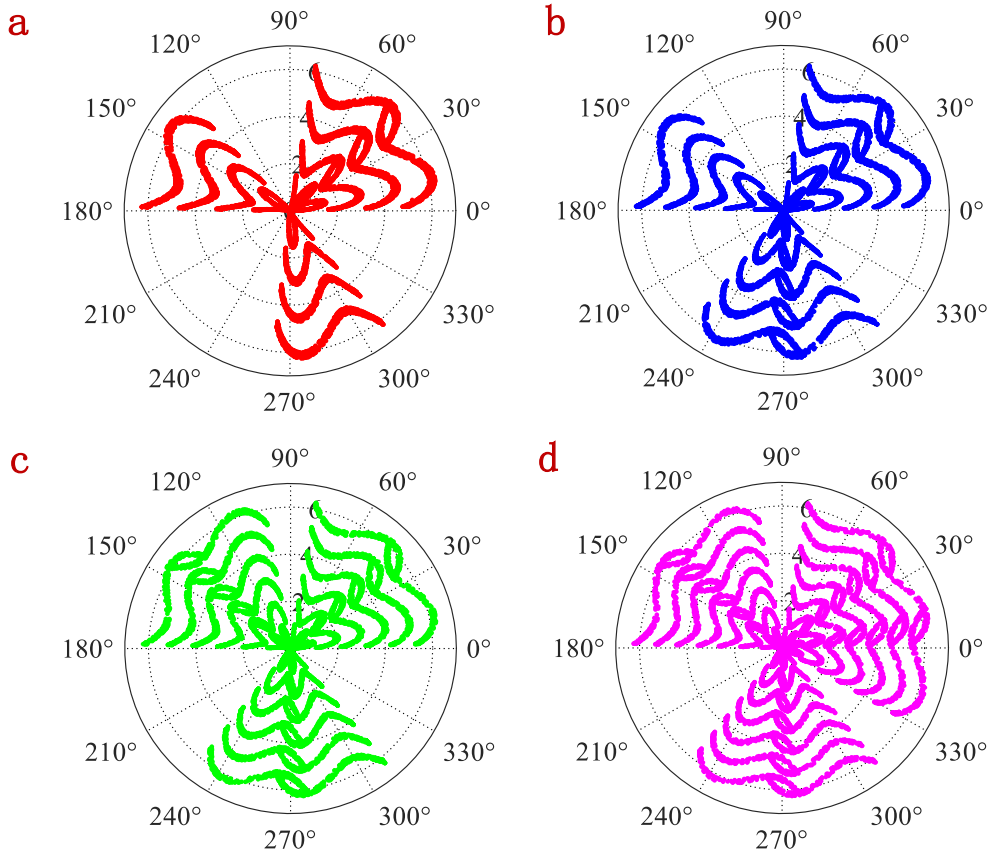


Figure 6. The multi-cavity chaotic attractors in the GCM6 system. (**a**) 4 × 4, (**b**) 5 × 5, (**c**) 6 × 6, (**d**) 7 × 7.

For the sequences generated by the one-dimensional chaotic system, this study constructs a multi-cavity attractor in the polar coordinate system of the phase space using the

combination (y_{n-1}, y_n), with the algorithmic parameter ρ set to 0.8. Through 3×4 and 4×4 grid configurations, grid attractors in polar coordinates were successfully constructed, with the results shown in Figure 7. It is observed that after the mapping transformation, the phase diagram is divided into an orderly and symmetrically distributed mesh structure in the polar coordinate space, which verifies the effectiveness of the method proposed in this study.

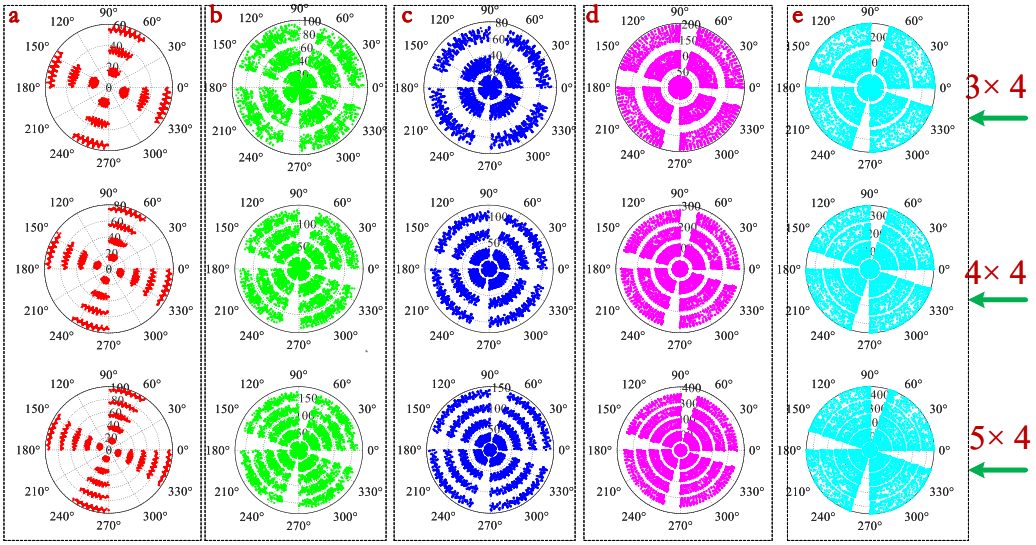


Figure 7. The grid multi-cavity attractors constructed based on different chaotic systems. (**a**) GCM1, (**b**) GCM2, (**c**) GCM3, (**d**) GCM4, (**e**) GCM5.

3.3. Comparison with the Existing Method

Compared with those methods for the design of multi-cavity chaotic maps, the method proposed in this paper indicates a more direct way. In current academic research, the design of discrete multi-cavity chaotic mapping typically employs staircase wave functions to achieve position migration, which is defined as [34]

$$g(x_n) = \begin{cases} \kappa \sum\limits_{k=1}^{N} \left[\operatorname{sgn}\left(\frac{N}{\kappa} x(n) + 2k - 1\right) + \right. \\ \left. \operatorname{sgn}\left(\frac{N}{\kappa} x(n) - 2k + 1\right) \right], \ \textit{Odd number} \\ \kappa \cdot \operatorname{sgn}\left(\frac{N}{\kappa} x(n)\right) + A \sum\limits_{k=1}^{N} \left[\operatorname{sgn}\left(\frac{N}{\kappa} x(n) + 2k - 1\right) + \right. \\ \left. \operatorname{sgn}\left(\frac{N}{\kappa} x(n) - 2k + 1\right) \right], \ \textit{Even number} \end{cases}, \tag{25}$$

where κ is the amplitude and N control the number of cavities. In many cases, this function incorporates the 2D Sine iterative chaotic map (2DSICM) with infinite collapse for model design, with the chaotic mapping defined as

$$\begin{cases} x_{n+1} = a \sin(\omega y_n) \sin\left(\frac{b}{x_n}\right) \\ y_{n+1} = a \sin(\omega x_{n+1}) \sin\left(\frac{b}{y_n}\right) + \kappa g(x_n) \end{cases}, \tag{26}$$

where $a = 1$ and $b = 10$. In this model, a also controls the number of cavities.

Here, a multi-cavity chaotic mapping model in Cartesian coordinates was constructed by integrating the designed controller into the system. The mathematical expression of the model is

$$\begin{cases} x_{n+1} = a \sin(\omega y_n) \sin\left(\frac{b}{x_n}\right) \\ y_{n+1} = a \sin(\omega x_{n+1}) \sin\left(\frac{b}{y_n}\right) + \kappa h(x_n, m) \end{cases} \tag{27}$$

where $\kappa = 2a$, m is related to the number of cavities. Under the condition of parameter $a = 1$, the phase diagram of the chaotic attractor for the two-dimensional self-excited chaotic map (2DSICM) is shown on the left side of Figure 8, exhibiting a cavity structure with two sinusoidal waveforms. After introducing the control parameter, the blue phase diagram illustrates the cases where $a = 1$ and the control parameter m takes values of 3 and 4, while the magenta phase diagram corresponds to the scenario where $m = a$, with m taking values of 2 and 3. From this, it can be observed that the system is capable of generating multi-cavity chaotic attractors with a $2a \times m$ grid structure.

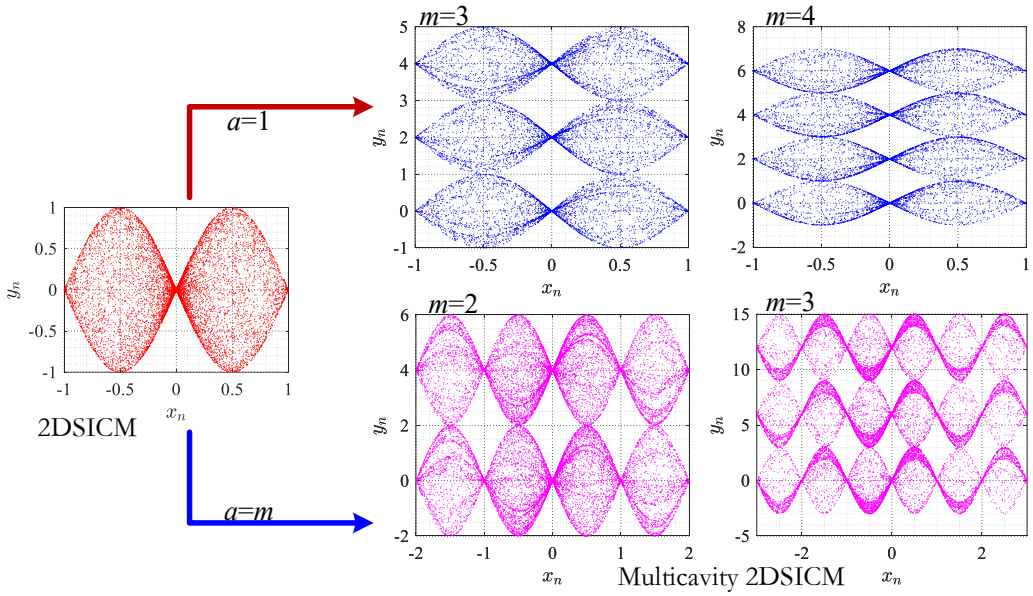


Figure 8. The application effect of the multi-cavity attractor generation algorithm proposed in this study in the Cartesian coordinate system.

3.4. Grid Cavity in the Cartesian Coordinate System

The multi-cavity structure in polar coordinates also exhibits multi-cavity characteristics in the Cartesian coordinate system, and there is a clear correspondence between the two. By combining the conversion formulas between polar and Cartesian coordinate systems Equation (13), when r in polar coordinates is dynamically folded through modulus operation to form multiple cavities, x and y will change in coordination with the variation of r, resulting in the formation of corresponding multi-cavity structures in the Cartesian coordinate system. As shown in Figure 9, in the polar coordinate system, the 5-ring multi-cavity attractor appears as a 5×5 grid multi-cavity attractor in the Cavendish coordinate axis.

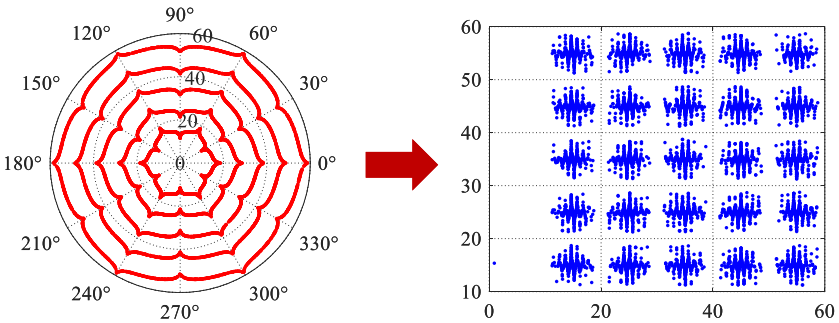


Figure 9. The grid multi-cavity attractor within the rectangular coordinate system corresponds to the ring-shaped multi-cavity attractor in the polar coordinate system.

3.5. On the Effect of the Fractional-Order Difference on the Multi-Cavity

3.5.1. Multi-Cavity with G-L Fractional-Order Difference

For a given G-L fractional-order discrete system, which is defined by [35]

$$ {}^{G}\Delta_{t_0}^{\alpha} y(t_n) = g(y(t_{n-1}), t_{n-1}), \tag{28} $$

thus, when its initial condition is $x(t_0)$, the solution of this system is denoted as

$$ y(t_n) = g(y(t_{n-1}), t_{n-1}) - \sum_{j=1}^{n-1} G_j^{(\alpha)} y(t_{n-j-1}). \tag{29} $$

where $G_j^{(\alpha)} = (-1)^j \begin{pmatrix} \alpha \\ j \end{pmatrix}$. It reflects the memory effect and historical dependence characteristics of fractional-order discrete systems in the time-recursive process.

Take the GCM*i* as an example, the G-L fractional-order GCM*i* is denoted as [35]

$$ y_n = R \cdot g(y_{n-1}) + \kappa_i \cdot h(y_{n-1}, m_i) - \sum_{j=1}^{n-1} G_j^{(\alpha)} y_{n-j-1} \tag{30} $$

where R is the system parameter, $g(\cdot)$ is the system function, and $\kappa_i \cdot h(y_{n-1}, m_i)$ controls the offset. For GCM1, $a_1 = 3$, $R = 5$, $\kappa_1 = 2m_1$ and $Num = 2$, phase diagrams of the system with $\alpha = 0.3$, 0.4, 0.5 and 0.6 are shown in Figure 10. It can be seen that as the fractional-order α gradually increases, the multi-cavity structural features in the model will gradually weaken and eventually disappear; at the same time, the fluctuation amplitude and variation range of the sequence also show a significant expansion trend. This indicates that the G-L fractional difference operator will cause damage to the multi-cavity attractor structure; although the system becomes more complex, this regular structure will be lost.

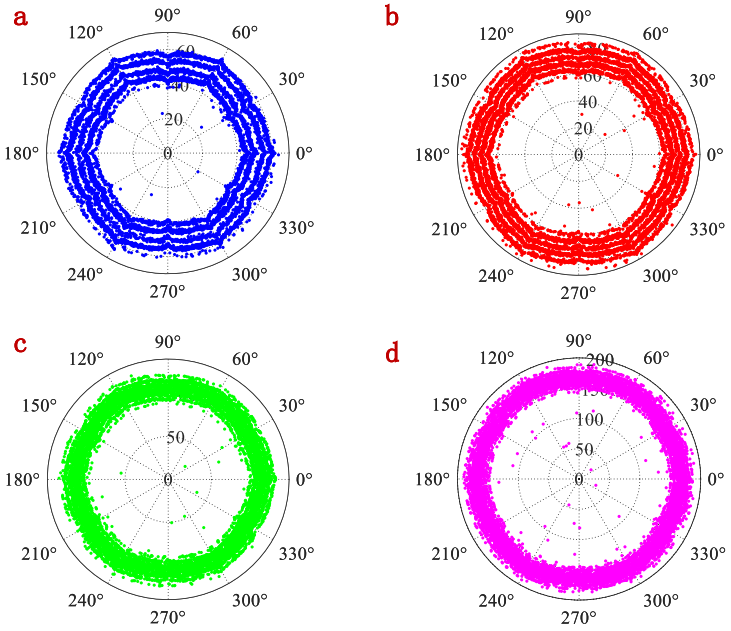


Figure 10. Phase diagrams of G-L fractional-order GCM1 under different differential orders. (**a**) $\alpha = 0.3$, (**b**) $\alpha = 0.4$, (**c**) $\alpha = 0.5$, (**d**) $\alpha = 0.6$.

3.5.2. Multi-Cavity with Caputo-like Fractional-Order Difference

Based on the introduction of the Caputo-like fractional difference operator [36], the definition of a discrete Caputo-like fractional-order system can be expressed as

$$ {}^{C}\Delta_{t_0}^{y}\varphi(t_n) = f(y(t_n), t_n + \alpha - 1) \tag{31} $$

where $t_n \in N_{t_0+m-\alpha}$. Its solution is given by

$$ y(t_n) = \begin{matrix} \sum_{k=0}^{n-1} \frac{(t_k - t_0)^{(k)}}{k!} \Delta^k y(t_0) \\ + \frac{1}{\Gamma(\alpha)} \sum_{s=t_0+n-\alpha}^{t_s - v} \frac{f(s+\alpha-1, y(s+\alpha-1))}{(t_s - \sigma(s))^{1-\alpha}} \end{matrix}, \tag{32} $$

where $\Delta^k y(t_0) = {}_k$, $k = 0, 1, \cdots, n-1$.

To introduce the Caputo-like fractional-order difference to the GCM*i*, it should be defined by [36]

$$ {}^{C}\Delta_{t_0}^{\alpha} y_n = g(y_{n-1}) + \kappa_i \cdot h(y_{n-1}, m_i) - y_{n-1}, \tag{33} $$

thus, when its initial condition is $y(t_0)$, the solution of this system is denoted as

$$ y_n = y_0 + \frac{1}{\Gamma(\alpha)} \sum_{j=1}^{n} C_j^{(\alpha)} [R \cdot g(y_{n-1}) + \kappa_i \cdot h(y_{n-1}, m_i) - y_{n-1}] \tag{34} $$

where

$$ C_j^{(\alpha)} = \begin{cases} \Gamma(\alpha), j = 0 \\ C_{j-1}^{(\alpha)} \frac{\alpha + j - 1}{j}, j = 1, 2, \cdots \end{cases}, \tag{35} $$

and it is a simplified calculation method for the memory modulation factor of the Caputo-like fractional difference operator.

Taking GCM1 as an illustration, let $a_1 = 3$, $R = 5$, $\kappa_1 = 2m_1$, and $Num = 2$. The phase diagrams of the system corresponding to $\alpha = 0.3, 0.4, 0.5$, and 0.6 are presented in Figure 11. Therefore, it can be seen that after introducing the Caputo-like fractional difference operator into the system model, the number of cavities in the system will significantly increase, thus breaking the simple structure of only two rings in the integer-order case.

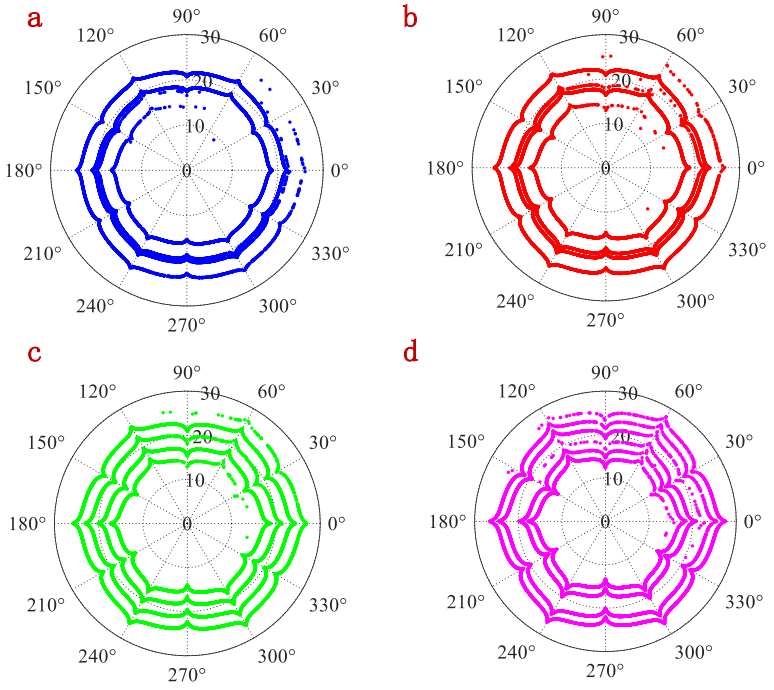


Figure 11. Phase diagrams of Caputo-like fractional-order GCM1 under different differential orders. (**a**) $\alpha = 0.3$, (**b**) $\alpha = 0.4$, (**c**) $\alpha = 0.5$, (**d**) $\alpha = 0.6$.

4. Performance of the Chaotic Maps

4.1. Fix Points and Stability

For the one-dimensional chaotic map with the form of $y_{n+1} = f(y_n)$, where $f(x)$ is a smooth differentiable function, suppose that there exits fix point y^*, the results of the system stability determination are as follows.

Firstly, the fix points, decided by $y^* = f(y^*)$, are those cross points of curves with the line $r = \theta$, and it is given by

$$\begin{cases} r = \theta \\ r_i = f_i(\theta), i = 1, \cdots, 5 \end{cases}' \tag{36}$$

where f_i is the system equation of CM_i. Figure 12a illustrates the distribution of intersection points between various one-dimensional system curves and oblique straight lines. Observations reveal that different systems possess specific fixed points, with notable variations in both the quantity and positioning of these fixed points. Taking the CM5 system as an example, this system possesses 9 fixed points. By applying numerical solution algorithms, we accurately calculated the values of these fixed points, which are -3.5777, -3.2215, -0.6971, -1.5214, 0.6003, 1.7698, 2.7277, 4.2563, 4.8241.

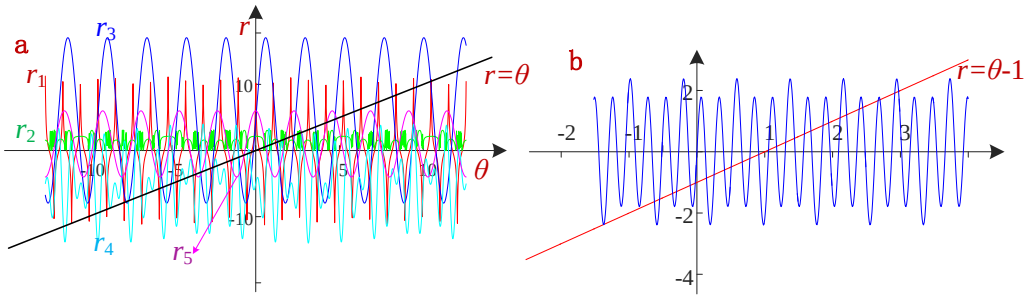


Figure 12. Illustration of the fixed points of different chaotic systems. (**a**) Distribution of fix points for systems CM1 to CM5; (**b**) Layout of stable points for the system CM6.

Secondly, in the stability analysis of one-dimensional chaotic mappings, the distribution of the derivative values of the system function at the fixed points is a decisive factor. Specifically, stability depends on whether the absolute value of the derivative is greater than or equal to 1. According to this criterion, the stability analysis can be divided into two major categories.

(1) When $|f'(y^*)| < 1$, the fixed point y^* is deemed stable.
(2) When $|f'(y^*)| > 1$, the fixed point y^* is considered unstable.

For the CM5 model, the system definition after derivative calculation is denoted as

$$f_5'(y^*) = 6.65b\cos(2.66y^*). \tag{37}$$

Based on the outcomes of the computational analysis, when the system chooses the fifth and sixth fixed points, the absolute value of the derivative of the function $f'(y^*)$ is less than 1; while for other fixed points, the absolute value of the function $f'(y^*)$ is greater than 1. Based on this, the system as a whole exhibits instability, meeting the conditions for the occurrence of chaotic phenomena.

Thirdly, in the context of a high-dimensional system, it is imperative to scrutinize the eigenvalues of the Jacobian matrix at fixed points. When the characteristic roots of the

system contain solutions with absolute values greater than one, it indicates that the system is in an unstable state and can generate chaotic phenomena. According to CM6, we have

$$\begin{cases} \theta^* - 1 = c_6 \sin b_6\theta^* + d_6 \sin a_6\theta^* \\ r^* = \theta^* - c_6 \sin b_6\theta^* \end{cases} \tag{38}$$

Based on the first equation of Equation (38), the analytical solution of θ^* can be obtained, and then the second equation is used to solve for r^*. Observing Figure 12b, there are approximately 30 fixed points in the system. For instance, when $\theta^* = 2.9724$, the characteristic root is $(\lambda_1, \lambda_2) = (-0.0238, -28.9324)$. It means that the system is unstable.

4.2. Bifurcations and LEs

The Lyapunov exponent is an important quantitative indicator for measuring the dynamic characteristics of a system, which characterizes the average exponential convergence or divergence rate between adjacent trajectories in the phase space. It is defined by [37]

$$Ly = \lim_{n\to\infty} \frac{1}{n} \sum_{i=0}^{n-1} \log \left| \frac{df(x)}{dx} \right|_{x_n}, \tag{39}$$

where n is the iteration number. Generally, it is equal to the length of the sequence. When the system dimension is greater than two, the QR decomposition method is employed to solve for multiple Lyapunov exponents (LEs).

Firstly, this study analyzed the bifurcation diagrams and Lyapunov exponents (LEs) of the CM1-CM5 systems under parameter variations, with the relevant results presented in Figure 13. Within the span of each parameter, 250 data points were uniformly distributed, meaning the step size for parameter variation was the parameter span divided by 250. Except for the varying parameter, the settings of other parameters are detailed in Table 1. The bifurcation diagrams and exponent spectra are displayed in the same figure but represented separately by the left and right vertical axes to indicate their respective value ranges.

- When parameter R exists in the system, the fluctuation range of the sequence increases as R grows. Except for the initial stage where the system is in a non-chaotic state when R is small, the subsequent parts are primarily in a chaotic state, and the maximum Lyapunov exponent spectrum increases with the rise of R.
- When other parameters of the system change, the scenarios vary: the fluctuation range remains unchanged but the values increase (Figure 13a), decrease (Figure 13d), or stay the same (Figure 13d), periodic fluctuation bifurcation diagram (Figure 13c), and the fluctuation range increases (Figure 13e).
- The correspondence between the exponent spectrum and the bifurcation diagram is consistent, indicating that the designed system exhibits rich dynamic behaviors.

Secondly, given that CM6 is a two-dimensional system containing four parameters, the analysis results exhibit uniqueness, as shown in Figure 14. Specifically, when parameters a_6 and b_6 vary, the fluctuation range and value domain of the sequence do not show significant changes, with only a few periodic windows observed and the system overall exhibiting chaotic behavior. Moreover, adjustments to parameters $c6$ and d_6 lead to an expansion of the sequence's fluctuation range, i.e., an increase in the size of the attractor. Finally, the study did not identify hyperchaotic phenomena in the system.

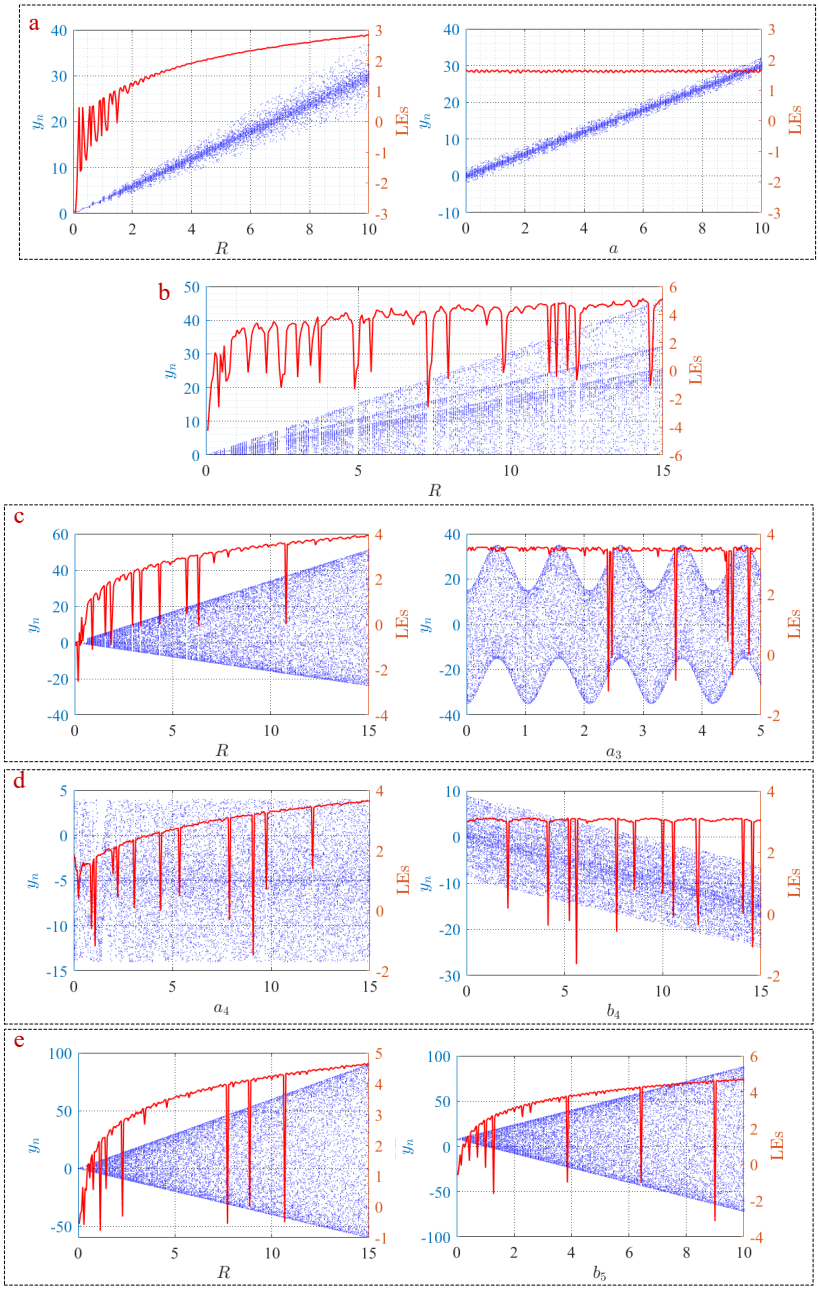


Figure 13. Analysis of bifurcation diagrams and Lyapunov exponent spectra under variations of different system parameters. (**a**) CM1, (**b**) CM2, (**c**) CM3, (**d**) CM4, (**e**) CM5.

4.3. Entropy and Complexity

This study employs three algorithms to quantitatively analyze the sequence complexity generated by different systems, specifically including Sample Entropy (SampEn) [38], Spectral Entropy (SE) [39], and the C_0 complexity measure algorithm [40]. Among these, SampEn belongs to the time-domain complexity analysis method, while SE and C_0 fall under the frequency-domain complexity analysis methods.

Consider a time series $\{x(n),\ n = 0,\ 1,\ 2,\ \cdots,\ N-1\}$ of length N. Define $x(n)$ as $x(n) = x(n) - \overline{x}$, where $\overline{x}$ represents the mean value of the time series. For a given integer number $\varphi(\varphi > 0)$, to calculate the SampEn, the vector is denoted as

$$X(i) = [x(i), x(i+1), \cdots, x(i+\varphi-1)], \tag{40}$$

where $i = 1, 2, \cdots, N - \varphi + 1$. Thus, Sample Entropy (SampEn) [38] is defined as:

$$\mathrm{SamEn}(\varphi, \delta, N) = \ln \Phi^{\varphi}(\delta) - \ln \Phi^{\varphi+1}(\delta), \tag{41}$$

where φ represents the dimension of the phase space, a non-negative integer not exceeding $N - 2$. Parameter δ signifies the similarity tolerance.

$$\Phi^{d}(\delta) = \frac{1}{N-d} \sum_{i=1}^{N-d} C_i^{d}(\delta), \tag{42}$$

where $d = \varphi$, $\varphi + 1$, and

$$C_i^{d}(\delta) = \frac{1}{N-d-1} \sum_{\substack{j=1 \\ j \neq i}}^{N-d} \#\left\{ d_{i,j}^{d} \leq \delta \right\}, \tag{43}$$

where $\#\{\cdot\}$ is the indicator function (1 if the condition holds, 0 otherwise). Meanwhile, the distance between two vectors of length d is the Chebyshev distance, which is denoted as

$$d_{i,j}^{d} = \max_{p=0,1,\ldots,d-1} \left| u(i+p) - u(j+p) \right|. \tag{44}$$

where $u(1), \ldots, u(N)$ come from phase space reconstruction with embedded dimension d.

The corresponding DFT (Discrete Fourier Transform) of the time series $\{x(n), n = 0, 1, 2, \cdots, N-1\}$ is defined by

$$X(k) = \sum_{n=0}^{N-1} x(n) e^{-j2\pi nk/N}, \tag{45}$$

where $k = 0, 1, \cdots, N-1$ and j is the imaginary unit. If the power of a discrete power spectrum with the k_{th} frequency is $|X(k)|^2$, then the "probability" of this frequency is defined as

$$P_k = \frac{|X(k)|^2}{\sum_{k=0}^{N/2-1} |X(k)|^2}. \tag{46}$$

Upon the application of the DFT, the summation is executed from $k = 0$ to $k = N/2 - 1$.

Firstly, the normalization entropy is designated as [39]

$$SE\left(x^N\right) = \frac{1}{\ln(N/2)} \sum_{k=0}^{N/2-1} P_k \ln(P_k), \tag{47}$$

where $ln(N/2)$ is the entropy of a completely random signal. Clearly, the more balanced the probability distribution, the greater the complexity (larger entropy) of the time series. A higher measuring value indicates greater complexity, and conversely.

Secondly, the C_0 algorithm is denoted as [40]

$$\begin{cases} \mathrm{C}_0(\rho, N) = \sum\limits_{n=0}^{N-1} |x(n) - \tilde{x}(n)|^2 / \sum\limits_{n=0}^{N-1} |x(n)|^2 \\ \tilde{x}(n) = \frac{1}{N} \sum\limits_{k=0}^{N-1} \tilde{X}(k) e^{j\frac{2\pi}{N}nk} = \frac{1}{N} \sum\limits_{k=0}^{N-1} \tilde{X}(k) W_N^{-nk} \\ \tilde{X}(k) = \begin{cases} X(k), if |X(k)|^2 > \rho G_N \\ 0, if |X(k)|^2 < \rho G_N \end{cases} \\ G_N = \frac{1}{N} \sum\limits_{k=0}^{N-1} |X(k)|^2 \end{cases}. \tag{48}$$

where ρ is the tolerance and N is the length of the time series. And $\rho = 15$ is chosen in this study. When exploring C_0 complexity algorithms, a positive correlation can be observed between the measure values and sequence complexity, meaning that an increase in measure values indicates an enhancement in sequence complexity, and vice versa.

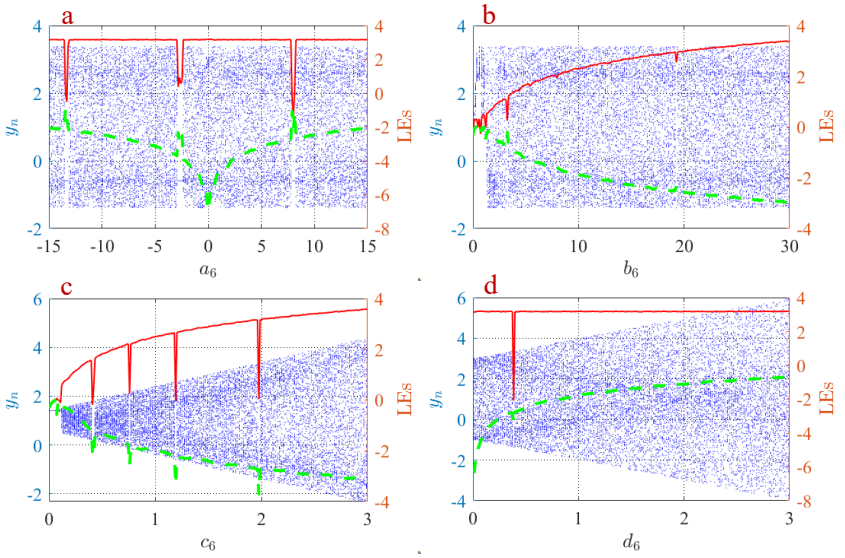


Figure 14. The complex dynamic behavior of the CM6 varies with different parameters. (**a**) a_6 varying, (**b**) b_6 varying, (**c**) c_6 varying, (**d**) d_6 varying.

In the process of calculating LEs, due to the involvement of modulo and rounding operations, it is unsuitable for derivative computations, thus preventing the calculation of the exponent spectrum for multi-cavity chaotic maps. However, this study further explores the evolution patterns of sequence complexity and analyzes the trend of sequence complexity with varying numbers of cavities. For the unidirectional one-dimensional multi-cavity chaotic maps (GCM1 to GCM5), this study conducts an in-depth analysis of the relationship between the multi-cavity control parameter m and complexity, with the results presented in Figure 15a–c. The analysis based on SampEn indicates that as (m) increases, the system complexity exhibits an upward trend; however, when m exceeds 10, and the measure value surpasses 2.5, the system complexity gradually stabilizes. Furthermore, the Shannon Entropy (SE) analysis results also demonstrate that increasing the number of cavities does not significantly enhance the system's complexity. Integrating the C0 complexity analysis results, a clear conclusion can be drawn as (m) increases, the system complexity generally tends to stabilize.

For GM6, the analysis results are shown in Figure 15d. m_1 represents the multi-cavity control parameter in the r coordinate direction, and m_2 represents the control parameter in the θ direction. Observing the figure, it can be seen that m_1 has a significant impact on the complexity of the system, while the complexity changes almost insignificantly with the variation of m_2. The trend of this change is consistent with the aforementioned complexity variation rule, further indicating that as the number of cavities in the r direction increases, the complexity will increase accordingly, but will eventually tend to a stable state.

Furthermore, this study analyzed the complexity of the grid multi-cavity chaotic attractor after the transformation of the one-dimensional chaotic mapping generated sequence through the scheme shown in Figure 4. The analysis results are presented in Figure 15e–g. The figure illustrates the regularity with the variation of parameter m1, while an averaging process was applied for different values when parameter m2 changes. The research found that increasing the number of multi-cavities along the r-axis can effectively enhance the system's complexity.

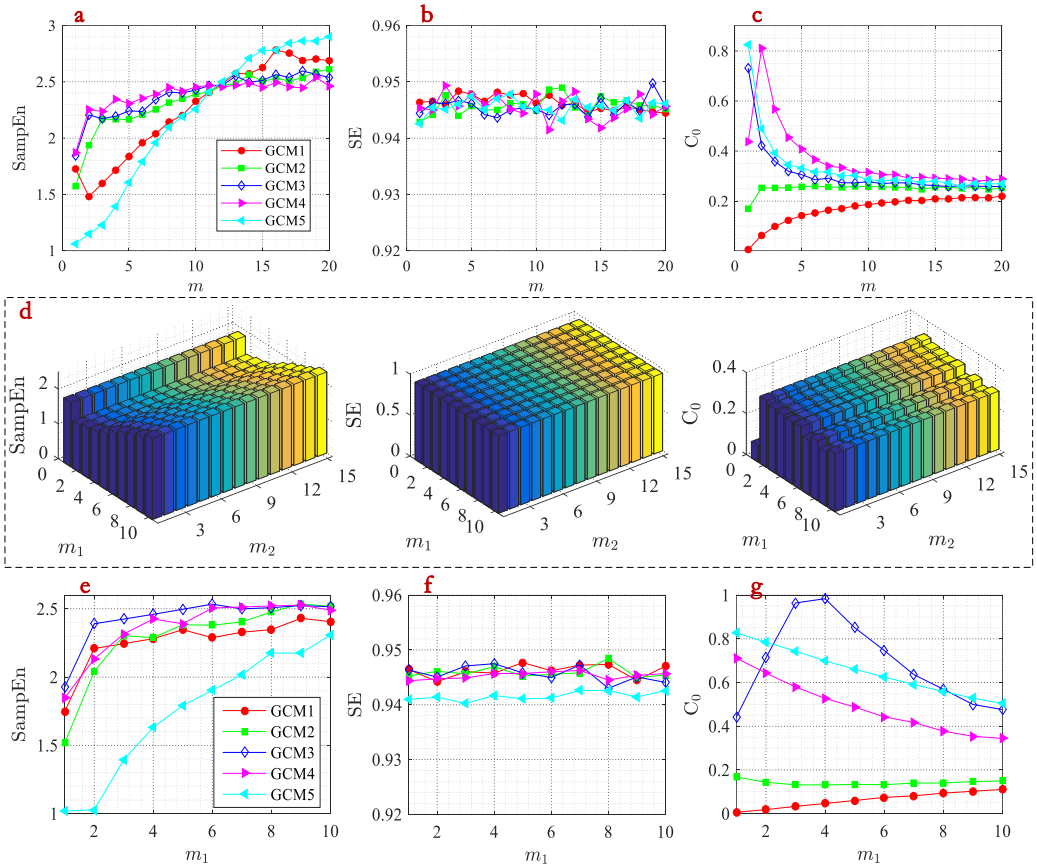


Figure 15. The complexity analysis results of the multi-cavity chaotic maps. (**a**) The variation law of SampEn complexity of different multi-cavity chaotic maps with the number of cavities (m), (**b**) The variation law of SE complexity of different multi-cavity chaotic maps with the number of cavities (m), (**c**) The variation law of C_0 complexity of different multi-cavity chaotic maps with the number of cavities (m), (**d**) The variation law of GCM6 complexity with m, (**e**) The variation law of SampEn complexity of grid multi-cavity chaotic attractors with $m_1 = m_2$, (**f**) The variation law of SE complexity of grid multi-cavity chaotic attractors with $m_1 = m_2$, (**g**) The variation law of C_0 complexity of grid multi-cavity chaotic attractors with $m_1 = m_2$.

5. Information Hiding and Applications

5.1. Information Hiding Algorithm

According to the multi-cavity mapping generation equation as given in Equation (14), where $h(x_n, m)$ is a positive integer between 0 and m. If the positive integer sequence generated by the $h(\cdot)$ function is replaced with an external input signal, such as an image signal, the multi-cavity chaotic mapping can be modulated by the external image signal. The resulting sequence will exhibit chaotic characteristics, thereby achieving the concealment of signals within the multi-cavity attractor mapping.

Figure 16 reveals a potential covert transmission strategy for image information. In the initial stage, the image is converted into a bitmap format, totaling eight images. By pairwise combination, data ranging from 0 to 3 is generated, which is then transformed into a one-dimensional sequence. Consequently, the final sequence has a length of $4MN$, where M and N represent the length and width of the image, respectively. Subsequently, based on an encryption sequence generated by a third-party chaotic mapping, a chaotic pseudo-random sequence of length $4MN$ is obtained. This sequence is utilized for encrypting and scrambling the image sequence.

Thirdly, the chaotic map defined by Equation (11) is used to embed information symbols $F_n \in \{0, 1, 2, 3\}$ into a transmitted signal y_n. At the receiver, the original symbols

are recovered without requiring channel coding, provided perfect synchronization of the initial condition y_0. The scheme is vulnerable to noise and initial condition mismatch due to the chaotic sensitivity.

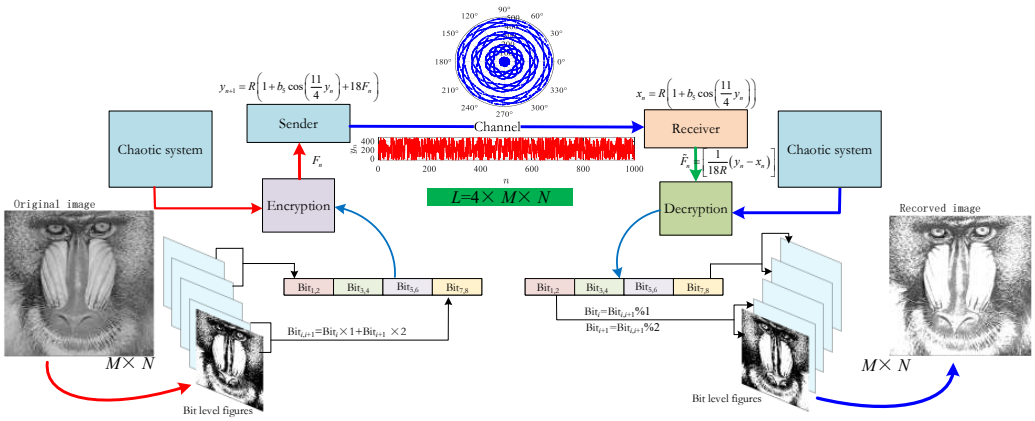


Figure 16. The schematic diagram of information hiding demonstrates the method of regulating the position of the system's iterative points through the pixel values of the image to conceal the image information within the multi-cavity attractor. Additionally, it also includes the information encryption algorithm based on chaos.

For each symbol F_n, the next state y_{n+1} is generated by

$$y_{n+1} = R\left(1 + b\cos\left(\frac{11}{4}y_n\right) + 18F_n\right). \tag{49}$$

Then the sequence $\{y_0, y_1, y_2, \ldots, y_N\}$ is transmitted over the channel.

At the receiver, the incoming samples y_n are processed sequentially. Using the known current sample y_n, the "clean" chaotic term (without information) is computed as

$$x_n = R\left(1 + b\cos\left(\frac{11}{4}y_n\right)\right). \tag{50}$$

And the information symbol is then recovered from y_{n+1}:

$$\tilde{F}_n = \text{round}\left(\frac{y_{n+1} - x_n}{18R}\right), \tag{51}$$

and finally clipped to the valid range:

$$\hat{F}_n = \max(0,\ \min(3,\ \tilde{F}_n)). \tag{52}$$

It should be noted that the initial value y_0 cannot be identical at both ends. In practice, a preamble with $F_n \equiv 0$ can be sent to let the receiver synchronize its chaotic oscillator to the transmitted sequence. Meanwhile, the channel adds white Gaussian noise with standard deviation σ, and the received signal is

$$r_n = y_n + \varepsilon\eta_n, \tag{53}$$

where $\eta_n \sim \mathcal{N}(0, \sigma^2)$ is the noise signal defined in (0, 1) and ε is the strength level. In this case, all occurrences of y_n in (50) and (51) are replaced by r_n. The sensitivity to noise is high; channel coding is recommended for reliable transmission. The pseudocode given in Algorithm 1 summarizes the complete transmission and recovery process.

Algorithm 1 Chaotic Communication with Quaternary Symbols

Parameters: $R \leftarrow 8.0$, $b \leftarrow 5.0$, $\sigma \leftarrow$ noise std
Input: information vector $\mathbf{F} = [F_1, \ldots, F_N]$, initial y_0
Output: recovered symbols $\hat{\mathbf{F}}$, symbol error rate SER

function TRANSMITTER($\mathbf{F}$, y_0)
    $y_1 \leftarrow y_0$
    for $n = 1$ to N **do**
        $y_{n+1} \leftarrow R\left(1 + b\cos(\frac{11}{4}y_n) + 18F_n\right)$
    end for
    return $\mathbf{y} = [y_1, y_2, \ldots, y_{N+1}]$
end function

function CHANNEL($\mathbf{y}$, σ)
    for $k = 1$ to $N + 1$ **do**
        $r_k \leftarrow y_k + \sigma \cdot \mathcal{N}(0, 1)$
    end for
    return $\mathbf{r}$
end function

function RECEIVER($\mathbf{r}$)
    for $n = 1$ to N **do**
        $x_n \leftarrow R\left(1 + b\cos(\frac{11}{4}r_n)\right)$
        $\tilde{F}_n \leftarrow \text{round}\left(\dfrac{r_{n+1} - x_n}{18R}\right)$
        $\hat{F}_n \leftarrow \max(0,\ \min(3,\ \tilde{F}_n))$
    end for
    return $\hat{\mathbf{F}}$
end function

Main:
$\mathbf{y}_{\text{tx}} \leftarrow \text{Transmitter}(\mathbf{F}, y_0)$
$\mathbf{r} \leftarrow \text{Channel}(\mathbf{y}_{\text{tx}}, \sigma)$
$\hat{\mathbf{F}} \leftarrow \text{Receiver}(\mathbf{r})$

Moreover, it should be pointed out that, in order to further ensure the security of the transmitted data, the data to be transmitted needs to be encrypted. Although this paper has performed simple XOR encryption on the data stream, in practical applications, more secure bit-level information encryption algorithms need to be designed.

Finally, this study conducted a further exploration of this algorithm and extended it to a general one-dimensional multi-cavity chaotic mapping. Based on a general one-dimensional multi-cavity chaotic mapping, its information loading equation is

$$y_{n+1} = R(f(y_n) + \kappa F_n). \tag{54}$$

where A is the step size, and $f(\cdot)$ is the system equation. At the receiving end, the following equation is executed

$$x_n = R \cdot f(y_n). \tag{55}$$

As a result, the information symbol is then recovered from y_{n+1}:

$$\tilde{F}_n = \text{round}\left(\frac{y_{n+1} - x_n}{\kappa \cdot R}\right), \tag{56}$$

and finally clipped to the valid range. That is to say, as long as appropriate parameters are selected, other chaotic maps can also be used for information hiding.

5.2. Simulations and Analysis

5.2.1. Simulations

Figure 17 presents the detailed procedural results of numerical simulation for Phoxinus phoxinus subsp. phoxinus, including the original image, bit-level map, data flow, signal transmission, recovered data flow, restored bit-level map, and reconstructed image. Overall, signal recovery is achievable through channel transmission with certain robustness against noise and parameter variations. This stems from the signal recovery process relying on how to extract quantized data, determined by the relative size of the attractor dimensions. However, as shown in the Phoxinus phoxinus subsp. phoxinus simulation results in Figure 17. Nevertheless, it demonstrates the effectiveness and application potential of the proposed multi-cavity attractor-based information hiding and recovery algorithm.

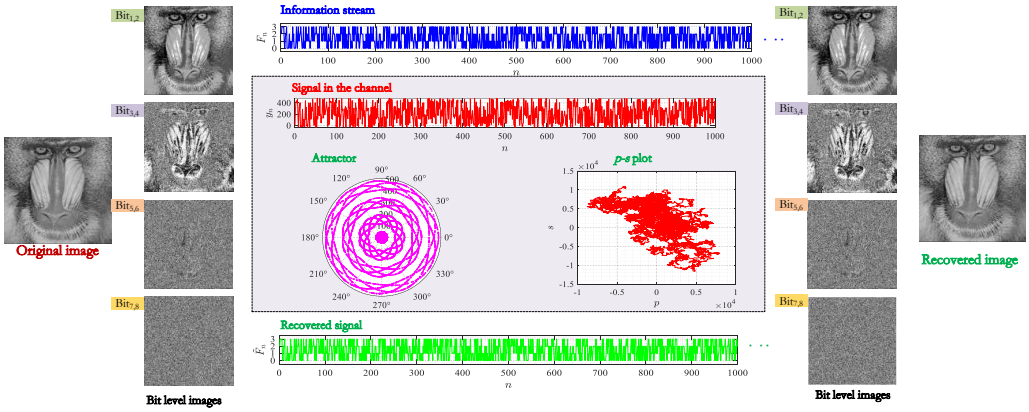


Figure 17. Present the results generated by each step in the implementation of the algorithm.

Regarding another issue, given that the jump positions of the original chaotic sequence are determined by image information, and image information typically belongs to deterministic information, it is necessary to further verify whether the sequence y_n transmitted in the channel still maintains chaotic characteristics. For this purpose, this study adopts the pseudo-spectrum graph (ps graph) of the 0-1 test to verify the existence of chaotic phenomena.

Figure 18 illustrates the impact of channel noise on the recovered image quality. As the noise intensity ε increases, both PSNR and SSIM exhibit a monotonic decline. For $\varepsilon \leq 0.3$, the PSNR remains above 40 dB, rendering the reconstructed image visually indistinguishable from the original. When ε approaches 0.44, the PSNR lies between 30 and 40 dB, still corresponding to good perceptual quality. Beyond this point, further increase in ε leads to severe degradation, with noticeable distortion becoming evident.

Table 2 reports the PSNR and SSIM values for five test images under two noise levels. When the noise intensity is $\varepsilon = 0.2$, the PSNR is infinite for the first two images and exceeds 67 dB for the others, while the SSIM remains exactly 1.000 in all cases. This indicates that the reconstruction is essentially identical to the original. At $\varepsilon = 0.3$, the PSNR drops to the range of 38–42 dB, yet all values stay above 38 dB; the SSIM also decreases slightly but remains above 0.96 for every image. These results demonstrate that the scheme preserves excellent image quality for moderate noise, with only minor perceptual degradation. Overall, the algorithm is robust to light channel noise and provides near-lossless recovery at very low noise levels.

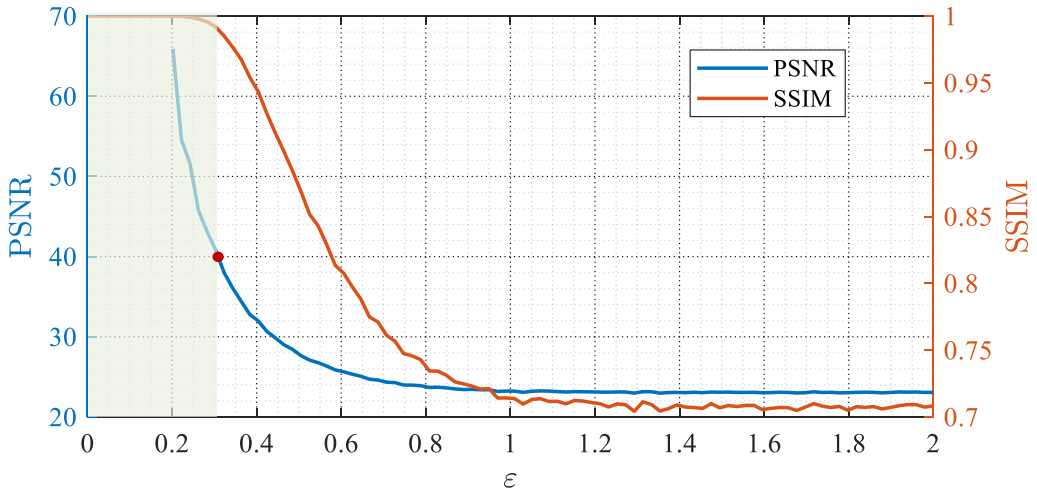


Figure 18. The quality of image restoration as the intensity of channel noise increases.

Table 2. Peak Signal-to-Noise Ratio (PSNR) and Structural Similarity Index (SSIM) under different image conditions and different noise intensities of channels.

Value / Figure / Index					
PSNR $\varepsilon = 0.2$	Inf	Inf	77.4875	67.7891	75.0899
$\varepsilon = 0.3$	41.9521	41.0233	40.3938	41.3099	38.4911
SSIM $\varepsilon = 0.2$	1.000	1.000	≈1	≈1	≈1
$\varepsilon = 0.3$	0.9870	0.9951	0.9855	0.9846	0.9676

5.2.2. Security Analysis

Firstly, we analyze the impact of channel bit width on communication quality, and from the perspective of data bit width, we examine the robustness of the system. Given that the data transmitted by the communication system is either y_n or $r_n = y_n + \varepsilon\eta_n$, we conducted a simplified experiment by imposing a limit on the computational precision of the channel to evaluate the system's precision requirements. The algorithm for limiting the data's significant digits is shown in Algorithm 2, which serves to restrict the number of significant figures. The analysis results are presented in Figure 19, from which it can be seen that after imposing a limit on the channel's significant digits, when *num* is greater than 3, the system can recover the original information with a PSNR greater than 40 and an SSIM greater than 0.7.

Algorithm 2 Round a number to *num* significant figures

```
function RoundToSignificant(value, num)
    if value = 0 then
        return 0
    else
        scale ← 10^(⌊log10(|value|)⌋+1−num)
        roundedValue ← round(value/scale) × scale
        return roundedValue
    end if
end function
```

Secondly, analyze the key space of the system. This part mainly affects the waveform of the signal transmitted through the channel. The shared key consists of the real numbers

$y_0 \in \mathcal{I}$ (the basin of f), R, and A. In a digital implementation with L-bit precision, the key space size is at least 2^{2L} (combining y_0 and R). Even for moderate precision ($L = 32$), the space is sufficiently large to resist brute-force attacks. More importantly, the chaotic sensitivity to initial conditions provides a fundamental security property.

Thirdly, based on the initial value sensitivity characteristic possessed by chaotic mappings, the following theory can be derived.

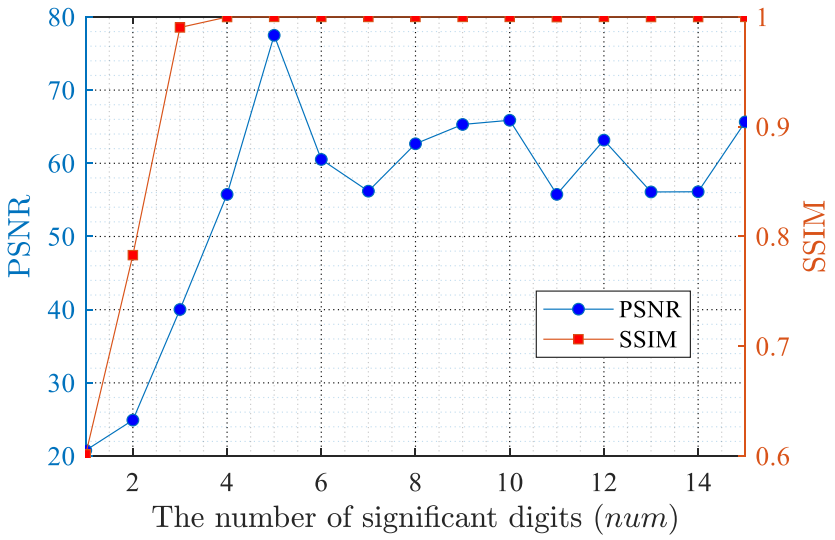


Figure 19. Present the results generated by each step in the implementation of the algorithm.

Theorem 1. *Let $\{y_n\}$ and $\{y'_n\}$ be two trajectories generated by the same map f and identical R, A, but with initial conditions satisfying $|y_0 - y'_0| = \delta > 0$. If f has a positive Lyapunov exponent $\lambda > 0$, then for large n the divergence $|y_n - y'_n|$ grows as $\delta e^{\lambda n}$ on average.*

Proof. The chaotic map f possesses a Lyapunov exponent $\lambda = \lim_{n\to\infty} \frac{1}{n} \sum_{i=0}^{n-1} \ln |f'(y_i)| > 0$. For two trajectories starting from y_0 and $y_0 + \delta$, the linearized error dynamics gives $|y_n - y'_n| \approx \delta e^{\lambda n}$ after n iterations. Since the recovery of F_n involves the subtraction $y_{n+1} - Rf(y_n)$, an error in y_n is amplified to $R|f(y_n) - f(y'_n)| \approx R|f'(y_n)||y_n - y'_n|$, which grows exponentially. Once this error becomes comparable to $AR/2$, the rounding operation in Equation (56) yields an incorrect symbol with high probability. □

Given that this information hiding scheme is constructed based on chaotic mapping, the signal transmitted in the channel is generated by the system, and only the value of the target signal is subjected to "translation" processing. Therefore, the initial value sensitivity and other characteristics of the nonlinear chaotic system can be continuously maintained, thereby providing a guarantee for information security.

Finally, the signal transmitted through the channel is a chaotic signal. The 0-1 test is a testing algorithm used to measure whether a time series exhibits chaos. Unlike the Lyapunov exponent, this algorithm does not require phase space reconstruction. For a given constant $\phi \in (0, \pi)$, one has [41]

$$\begin{cases} p_n = \sum_{j=1}^{n} y_j \cos(j\phi) \\ s_n = \sum_{j=1}^{n} y_j \sin(j\phi) \end{cases}, \tag{57}$$

where n takes values of $1, 2, \cdots$. We can draw a graph with p and s as the horizontal and vertical axes, respectively. The trajectory shown in this graph can reflect the characteristics

of the chaotic phenomenon. As can be seen from Figure 17, the information transmitted in the channel is a chaotic signal.

5.2.3. Influence of Fractional Difference on Data Hiding

The fractional-order difference operator has a memory effect, and its solution process is not a simple iterative equation. This implies that the solution methods at the sending end and the receiving end need to be carried out according to the relevant definitions of the fractional-order difference operator. Therefore, if the fractional-order system is introduced into the existing information hiding algorithm, it can be predicted that it will not be helpful for the data recovery of the information hiding algorithm, or a special hidden algorithm needs to be designed for the fractional-order system.

The G-L fractional-order difference operator may lead to damage to the multi-chamber structure. As depicted in Figure 10, with the increase of the fractional-order α, the multi-chamber structure gradually weakens until it vanishes, resulting in the malfunction of the "separation container" for information embedding. Consequently, the embedded information bits become confused, ultimately reducing the accuracy of information recovery.

The Caputo-like fractional-order difference operator will increase the number of multi-chambers, as shown in Figure 11. Although it does not cause damage to the multi-chamber structure, but an excessive number of multi-chambers will increase the difficulty of chamber distinction during information embedding, leading to information mis-embedding and reducing the recovery accuracy.

6. Conclusions

This paper proposes a design framework for polar coordinate multi-cavity chaotic mapping based on nonlinear curves and modular operations, successfully addressing the issues of simple structure and limited parameter space in existing polar coordinate chaotic mappings. By introducing complex deformations through nonlinear curves and achieving dynamic folding with modular operations, the generated chaotic mapping can form controllable numbers, sizes, and shapes of cavity structures in the phase space. Meanwhile, the designed algorithm is also applicable to the generation of multi-cavity chaotic attractors in the Cartesian coordinate system. Simulation analysis of dynamic characteristics shows that each mapping has high Lyapunov exponents, complex bifurcation behaviors, and the grid-like attractors have relatively higher complexity, meeting the requirements of cryptographic applications. At the application level, the multi-cavity structure is used for data hiding: cavities serve as isolated regions to embed information, and chaotic dynamics ensure data confusion and security. The proposed transmission scheme modulates image signals into chaotic sequences, and the receiving end recovers the information through inverse operations. Experiments verify the feasibility of the scheme.

Author Contributions: Conceptualization, B.Y. and S.B.; methodology, S.H.; software, S.H.; validation, B.Y. and S.B.; formal analysis, S.H.; investigation, S.H.; resources, S.H.; data curation, S.H.; writing—original draft preparation, B.Y.; writing—review and editing, S.H.; visualization, S.H. and S.B.; supervision, S.H.; project administration, S.H.; funding acquisition, B.Y. and S.H. All authors have read and agreed to the published version of the manuscript.

Funding: This research was funded by the Natural Science Foundation of Hunan Province (No. 2025JJ70215, 2022JJ50191).

Data Availability Statement: The original contributions presented in this study are included in the article. Further inquiries can be directed to the corresponding author.

Acknowledgments: We thank the associate editor and the reviewers for their useful feedback that improved this paper.

Conflicts of Interest: The authors declare no conflicts of interest.

References

1. Li, M.; Wang, M.; Fan, H.; An, K.; Liu, G. A novel plaintext-related chaotic image encryption scheme with no additional plaintext information. *Chaos Solitons Fractals* **2022**, *158*, 111989.
2. Borges, V.S.; Silva, M.T.; Eisencraft, M. Chaotic properties of an FIR filtered Hénon map. *Commun. Nonlinear Sci. Numer. Simul.* **2024**, *131*, 107845. [CrossRef]
3. Li, S.; Wu, Y.; Gao, L.; Li, T.; Zhang, Q.; Shen, Y.; Yang, Z. A high throughput pseudo-random number generator driven by four-dimensional discrete hyper-chaotic system. *Electron. Lett.* **2023**, *59*, el2950. [CrossRef]
4. Naik, R.B.; Singh, U. A review on applications of chaotic maps in pseudo-random number generators and encryption. *Ann. Data Sci.* **2024**, *11*, 25–50.
5. Sriram, G.; Ali, A.M.A.; Natiq, H.; Ahmadi, A.; Rajagopal, K.; Jafari, S. Dynamics of a novel chaotic map. *J. Comput. Appl. Math.* **2024**, *436*, 115453.
6. Zhang, L.; Li, Z.; Peng, Y. A hidden grid multi-scroll chaotic system coined with two multi-stable memristors. *Chaos Solitons Fractals* **2024**, *185*, 115109.
7. Ding, P.; Geng, P.; Hu, W. A new controllable multi-wing chaotic system: Applications in high-security color image encryption. *J. Supercomput.* **2025**, *81*, 108. [CrossRef]
8. Bao, H.; Xi, M.; Wang, N.; Xu, Q.; Bao, B. Designing multi-cavity chaotic maps via multistage step state extension. *Nonlinear Dyn.* **2024**, *112*, 12521–12535. [CrossRef]
9. Ye, X.; Wang, X.; Gao, S.; Mou, J.; Wang, Z. A new random diffusion algorithm based on the multi-scroll Chua's chaotic circuit system. *Opt. Lasers Eng.* **2020**, *127*, 105905.
10. Wang, N.; Li, C.; Bao, H.; Chen, M.; Bao, B. Generating multi-scroll Chua's attractors via simplified piecewise-linear Chua's diode. *IEEE Trans. Circuits Syst. I Regul. Pap.* **2019**, *66*, 4767–4779.
11. Li, F.; Zeng, J. Multi-scroll attractor and multi-stable dynamics of a three-dimensional jerk system. *Energies* **2023**, *16*, 2494. [CrossRef]
12. Lu, R.; Chen, Z.; Lu, L.; Bao, B. Designing multi-double-scroll jerk chaotic oscillators based on attractor modulators. *Chaos Solitons Fractals* **2024**, *187*, 115362. [CrossRef]
13. Yu, S.; Lu, J.; Leung, H.; Chen, G. Design and implementation of n-scroll chaotic attractors from a general jerk circuit. *IEEE Trans. Circuits Syst. I Regul. Pap.* **2005**, *52*, 1459–1476.
14. Tang, Z.L.; Yu, S.M. Multi-scroll chaotic system based on even-symmetric step-wave sequence control. *Appl. Mech. Mater.* **2013**, *340*, 760–766.
15. Xiao, Y.; Sun, K.; He, S. Constructing chaotic map with multi-cavity. *Eur. Phys. J. Plus* **2020**, *135*, 21. [CrossRef]
16. Zhu, W.; Sun, K.; He, S.; Wang, H.; Liu, W. A class of m-dimension grid multi-cavity hyperchaotic maps and its application. *Chaos Solitons Fractals* **2023**, *170*, 113370. [CrossRef]
17. Zhao, Q.; Bao, H.; Zhang, X.; Wu, H.; Bao, B. Complexity enhancement and grid basin of attraction in a locally active memristor-based multi-cavity map. *Chaos Solitons Fractals* **2024**, *182*, 114769.
18. Sun, H.; Liu, L.; Guo, A. Iteration Logistic Map Dynamics in the Polar Coordinates. *Fractals* **1998**, *6*, 11–22. [CrossRef]
19. Li, Y.X.; Wang, J.S.; Zhang, S.W.; Zhang, S.H.; Guan, X.Y.; Ma, X.R. Arithmetic optimization algorithm with cosine composite chaotic mapping in polar coordinate system for economic load dispatching problems in power systems. *Appl. Soft Comput.* **2025**, *175*, 113039. [CrossRef]
20. Jain, K.; Aji, A.; Krishnan, P. Medical image encryption scheme using multiple chaotic maps. *Pattern Recognit. Lett.* **2021**, *152*, 356–364. [CrossRef]
21. Benkouider, K.; Sambas, A.; Bonny, T.; Al Nassan, W.; Moghrabi, I.A.; Sulaiman, I.M.; Hassan, B.A.; Mamat, M. A comprehensive study of the novel 4D hyperchaotic system with self-exited multistability and application in the voice encryption. *Sci. Rep.* **2024**, *14*, 12993. [CrossRef]
22. Dong, Y.; Yan, R.; Yin, C. An adaptive robust watermarking scheme based on chaotic mapping. *Sci. Rep.* **2024**, *14*, 24735. [CrossRef] [PubMed]
23. Yang, Y.; Chang, R.; Feng, X.; Li, P.; Chen, Y.; Zhang, H. An n-dimensional chaotic map with application in reversible data hiding for medical images. *Entropy* **2024**, *26*, 254. [CrossRef] [PubMed]
24. Zang, H.; Fu, H.; Huang, L.; Lei, T.; He, S. Design chaotic maps with elegance of mathematical equations and strengthened by the discrete memristor. *Chaos* **2025**, *35*, 063114. [CrossRef]
25. Liu, W.; Sun, K.; Wang, H.; Li, B. The modular modulation chaotification map and its hardware implementation. *IEEE Trans. Instrum. Meas.* **2024**, *73*, 2002109. [CrossRef]
26. Hua, Z.; Zhu, Z.; Yi, S.; Zhang, Z.; Huang, H. Cross-plane colour image encryption using a two-dimensional logistic tent modular map. *Inf. Sci.* **2021**, *546*, 1063–1083. [CrossRef]

27. Moulin, P.; O'Sullivan, J.A. Information-theoretic analysis of information hiding. *IEEE Trans. Inf. Theory* **2003**, *49*, 563–593. [CrossRef]
28. Amin, M.M.; Salleh, M.; Ibrahim, S.; Katmin, M.R.; Shamsuddin, M. Information hiding using steganography. In *Proceedings of the 4th National Conference of Telecommunication Technology, 2003. NCTT 2003 Proceedings*; IEEE: Piscataway, NJ, USA, 2003; pp. 21–25.
29. Öztürk, İ.; Kılıç, R. Digitally generating true orbits of binary shift chaotic maps and their conjugates. *Commun. Nonlinear Sci. Numer. Simul.* **2018**, *62*, 395–408. [CrossRef]
30. Farschi, S.M.R.; Farschi, H. A novel chaotic approach for information hiding in image. *Nonlinear Dyn.* **2012**, *69*, 1525–1539. [CrossRef]
31. Nasr, M.A.; El-Shafai, W.; Abdel-Salam, N.; El-Rabaie, E.S.M.; El-Fishawy, A.S.; El-Samie, F.E.A. Efficient information hiding in medical optical images based on piecewise linear chaotic maps. *J. Opt.* **2023**, *52*, 1852–1866. [CrossRef]
32. Guang, Y.; Ding, Q. Dynamics analysis of a novel parametrically controllable symmetric multi-scroll chaotic system and FPGA design of an image encryption system. *Chaos Solitons Fractals* **2024**, *188*, 115572. [CrossRef]
33. Anitha, R.; Vijayalakshmi, B. Image Encryption Using Multi-Scroll Attractor and Chaotic Logistic Map. *Comput. Mater. Contin.* **2022**, *72*, 3447. [CrossRef]
34. He, S.; Banerjee, S. Multicavity formations and complexity modulation in a hyperchaotic discrete system. *Phys. A* **2018**, *490*, 366–377. [CrossRef]
35. Huang, L.; Wang, L.; Shi, D. Discrete fractional order chaotic systems synchronization based on the variable structure control with a new discrete reaching-law. *IEEE/CAA J. Autom. Sin.* **2016**, 1–7. [CrossRef]
36. Abdeljawad, T.; Baleanu, D. Fractional Differences and Integration by Parts. *J. Comput. Anal. Appl.* **2011**, *13*, 574–582.
37. Sandri, M. Numerical calculation of Lyapunov exponents. *Math. J.* **1996**, *6*, 78–84.
38. Chen, W.; Zhuang, J.; Yu, W.; Wang, Z. Measuring complexity using fuzzyen, apen, and sampen. *Med. Eng. Phys.* **2009**, *31*, 61–68. [CrossRef]
39. Zaccarelli, N.; Li, B.L.; Petrosillo, I.; Zurlini, G. Order and disorder in ecological time-series: Introducing normalized spectral entropy. *Ecol. Indic.* **2013**, *28*, 22–30. [CrossRef]
40. Cai, Z.; Sun, J. Convergence of C0 complexity. *Int. J. Bifurc. Chaos* **2009**, *19*, 977–992. [CrossRef]
41. Gottwald, G.A.; Melbourne, I. The 0-1 test for chaos: A review. In *Chaos Detection and Predictability*; Springer: Berlin/Heidelberg, Germany, 2016; pp. 221–247.

Disclaimer/Publisher's Note: The statements, opinions and data contained in all publications are solely those of the individual author(s) and contributor(s) and not of MDPI and/or the editor(s). MDPI and/or the editor(s) disclaim responsibility for any injury to people or property resulting from any ideas, methods, instructions or products referred to in the content.